



# MagAO-X and HST High-contrast Imaging of the AS209 Disk at H $\alpha$

Gabriele Cugno<sup>1</sup>, Yifan Zhou<sup>2</sup>, Thanawuth Thanathibodee<sup>3</sup>, Per Calissendorff<sup>1</sup>, Michael R. Meyer<sup>1</sup>, Suzan Edwards<sup>4</sup>, Jaehan Bae<sup>5</sup>, Myriam Benisty<sup>6,7</sup>, Edwin Bergin<sup>1</sup>, Matthew De Furio<sup>1</sup>, Stefano Facchini<sup>8</sup>, Jared R. Males<sup>9</sup>, Laird M. Close<sup>9</sup>, Richard D. Teague<sup>10</sup>, Olivier Guyon<sup>9,11,12,13</sup>, Sebastiaan Y. Haffert<sup>9,17</sup>, Alexander D. Hedglen<sup>11</sup>, Maggie Kautz<sup>11</sup>, Andrés Izquierdo<sup>14,15</sup>, Joseph D. Long<sup>9</sup>, Jennifer Lumbres<sup>11</sup>, Avalon L. McLeod<sup>11</sup>, Logan A. Pearce<sup>9</sup>, Lauren Schatz<sup>16</sup>, and Kyle Van Gorkom<sup>9</sup>

<sup>1</sup> Department of Astronomy, University of Michigan, Ann Arbor, MI 48109, USA; [gcugno@umich.edu](mailto:gcugno@umich.edu)

<sup>2</sup> Department of Astronomy, The University of Texas at Austin, 2515 Speedway, Stop C1400, Austin, TX 78712, USA

<sup>3</sup> Institute for Astrophysical Research, Department of Astronomy, Boston University, Boston, MA 02215, USA

<sup>4</sup> Five College Astronomy Department, Smith College, Northampton, MA 01063, USA

<sup>5</sup> Department of Astronomy, University of Florida, Gainesville, FL 32611, USA

<sup>6</sup> Laboratoire Lagrange, Université Côte d'Azur, CNRS, Observatoire de la Côte d'Azur, F-06304 Nice, France

<sup>7</sup> Univ. Grenoble Alpes, CNRS, IPAG, F-38000 Grenoble, France

<sup>8</sup> Università degli Studi di Milano, via Giovanni Celoria 16, I-20133 Milano, Italy

<sup>9</sup> Steward Observatory, University of Arizona, Tucson, AZ 85179, USA

<sup>10</sup> Department of Earth, Atmospheric, and Planetary Sciences, Massachusetts Institute of Technology, Cambridge, MA 02139, USA

<sup>11</sup> James C. Wyant College of Optical Sciences, University of Arizona, 1630 E University Blvd, Tucson, AZ 85719, USA

<sup>12</sup> National Astronomical Observatory of Japan, Subaru Telescope, National Institutes of Natural Sciences, Hilo, HI 96720, USA

<sup>13</sup> Astrobiology Center, National Institutes of Natural Sciences, 2-21-1 Osawa, Mitaka, Tokyo, JAPAN

<sup>14</sup> European Southern Observatory, Karl-Schwarzschild-Str. 2, D-85748 Garching bei München, Germany

<sup>15</sup> Leiden Observatory, Leiden University, P.O. Box 9513, 2300 RA Leiden, The Netherlands

<sup>16</sup> Air Force Research Laboratory, Directed Energy Directorate, Space Electro-Optics Division, Starfire Optical Range, Kirtland Air Force Base, NM 87117, USA

Received 2023 February 7; revised 2023 August 9; accepted 2023 August 22; published 2023 September 19

## Abstract

The detection of emission lines associated with accretion processes is a direct method for studying how and where gas giant planets form, how young planets interact with their natal protoplanetary disk, and how volatile delivery to their atmosphere takes place. H $\alpha$  ( $\lambda = 0.656 \mu\text{m}$ ) is expected to be the strongest accretion line observable from the ground with adaptive optics systems, and is therefore the target of specific high-contrast imaging campaigns. We present MagAO-X and Hubble Space Telescope (HST) data obtained to search for H $\alpha$  emission from the previously detected protoplanet candidate orbiting AS209, identified through Atacama Large Millimeter/submillimeter Array observations. No signal was detected at the location of the candidate, and we provide limits on its accretion. Our data would have detected an H $\alpha$  emission with  $F_{\text{H}\alpha} > 2.5 \pm 0.3 \times 10^{-16} \text{ erg s}^{-1} \text{ cm}^{-2}$ , a factor 6.5 lower than the HST flux measured for PDS70 b. The flux limit indicates that if the protoplanet is currently accreting it is likely that local extinction from circumstellar and circumplanetary material strongly attenuates its emission at optical wavelengths. In addition, the data reveal the first image of the jet north of the star as expected from previous detections of forbidden lines. Finally, this work demonstrates that current ground-based observations with extreme adaptive optics systems can be more sensitive than space-based observations, paving the way to the hunt for small planets in reflected light with extremely large telescopes.

*Unified Astronomy Thesaurus concepts:* [Exoplanet formation \(492\)](#); [Exoplanet detection methods \(489\)](#); [Direct imaging \(387\)](#); [Exoplanet astronomy \(486\)](#)

## 1. Introduction

In recent years observations by the Atacama Large Millimeter/submillimeter Array (ALMA) and high-contrast imagers including SPHERE and GPI revealed that circumstellar disks are highly structured, with gaps, rings, and spirals being among the most important observable features (e.g., Andrews et al. 2018; Avenhaus et al. 2018; Tschudi & Schmid 2021; Bae et al. 2022a; Benisty et al. 2022). While other explanations have been proposed (e.g., snowlines or turbulence; Flock et al. 2015; Zhang et al. 2015), it is widely accepted that at least some of these structures are the result of the interaction with forming planets. This hypothesis is supported by the direct

detection of two confirmed protoplanets in the cavity of the transition disk PDS70 (Keppler et al. 2018; Haffert et al. 2019). However, despite significant observational efforts, no other confirmed planet in the cavities of other disks has been detected, neither in the infrared (IR; Asensio-Torres et al. 2021; Cugno et al. 2023) nor in the emission lines associated with accretion (Cugno et al. 2019; Xie et al. 2020; Zurlo et al. 2020; Follette et al. 2022; Huélamo et al. 2022). Two candidates have been directly detected through H $\alpha$  emission (LkCa15 b and AB Aur b; Sallum et al. 2015; Currie et al. 2022): the first has never been redetected, and near-infrared (NIR) observations suggest it could be a reprocessed scattered light feature (Currie et al. 2019), while the second one shows H $\alpha$  emission consistent with scattered light from the disk (Zhou et al. 2022) and requires further investigation.

An alternative method for inferring the existence of protoplanets and studying their formation is to examine the effect they have on the disk structure (Pinte et al. 2022). Indeed, young gas giant planets leave observational traces on

<sup>17</sup> NASA Hubble Fellow.

the velocity field of the surrounding gas due to their gravitational force, manifesting as kinks (Pinte et al. 2018, 2020), Doppler flips (Casassus & Pérez 2019), deviations from Keplerian velocity (Teague et al. 2018, 2021), or molecular emission line broadening along the planet orbit (Dong et al. 2019; Izquierdo et al. 2022).

AS209 (alternative name V 1121 Oph) is a young ( $\approx 1$ –2 Myr; Andrews et al. 2009) K5 ( $V = 11.3$  mag) star with a mass of  $1.2 M_{\odot}$  (Öberg et al. 2021; Teague et al. 2021). Fernandez et al. (1995) measured the  $H\alpha$  flux of the star to be  $8.4 \times 10^{-12} \text{ erg s}^{-1} \text{ cm}^{-2}$ , which translates in a mass accretion rate of  $\dot{M}_{\text{acc}} = 10^{-8.2} M_{\odot} \text{ yr}^{-1}$  when using the line luminosity versus accretion luminosity relationship from Fang et al. (2009). This value is in strong agreement with the mass accretion rate of  $\dot{M}_{\text{acc}} = 10^{-8.3} M_{\odot} \text{ yr}^{-1}$  obtained by Fang et al. (2018) using multiple emission line luminosities other than  $H\alpha$ . It is surrounded by a well-studied protoplanetary disk ( $i = 35^{\circ} \pm 0^{\circ}.1$ ; Huang et al. 2018) that has been the subject of several major surveys such as DSHARP (Andrews et al. 2018; Guzmán et al. 2018; Huang et al. 2018), DARTTS-S (Avenhaus et al. 2018), and MAPS (Öberg et al. 2021). As part of the MAPS program, Bae et al. (2022b) identified a candidate circumplanetary disk (CPD) detected in  $^{13}\text{CO}$  within a gap at  $\sim 200$  au previously identified in  $^{12}\text{CO}$  and scattered light observations (Avenhaus et al. 2018; Guzmán et al. 2018). Subsequent kinematic analysis of the molecular line data revealed disk winds emerging from the gap around the candidate, showing a complex interplay between forming planets and disk winds (Galloway-Sprietsma et al. 2023; Izquierdo et al. 2023). A wind from the central star was also inferred through high-resolution spectroscopy of forbidden lines (Fang et al. 2018; Banzatti et al. 2019).

In this paper we search for  $H\alpha$  emission from the the CPD candidate orbiting AS209 with the Magellan Adaptive Optics eXtreme (MagAO-X) instrument (Males et al. 2022a) and with Hubble Space Telescope (HST)/WFC3/UVIS. MagAO-X is a new high-contrast imaging instrument that pushes extreme adaptive optics to visible wavelengths (Close et al. 2018; Males et al. 2018, 2022a), including  $H\alpha$  (Close 2020). MagAO-X is the successor to MagAO (Close et al. 2014b) and has an increased number of controllable modes (1600 versus 300), AO loop speed (2 kHz versus 1 kHz), and sensitivity (twice the throughput at  $H\alpha$ ). The data reveal a stellar jet at short separations, while no localized  $H\alpha$  emission at the location of the CPD candidate or anywhere else within the disk is detected. This paper is structured as follows: in Section 2 we present the MagAO-X and HST observations and in Section 3 we detail our data reductions. The main results are reported in Section 4 and discussed in Section 5. The conclusions of our work can be found in Section 6.

## 2. Observations

### 2.1. MagAO-X

AS209 was observed with the MagAO-X instrument at the Las Campanas Observatory on 2022 April 17 and 2022 April 20. The observing conditions were very different between the two nights. On April 17, data were taken under very stable conditions, with seeing  $< 0''.5$  for most of the night, air-mass  $< 1.2$ , and photometric sky. Conversely, due to extremely unstable atmospheric conditions on April 20, the second set of

data was not usable. As a result, this manuscript focuses solely on the data obtained on April 17.

AS209 was observed in  $H\alpha$  dual-band imaging mode, which involves splitting the light into the  $H\alpha$  ( $\lambda_c = 0.656 \mu\text{m}$ ,  $\Delta\lambda = 9 \text{ nm}$ ) and nearby continuum (Cnt;  $\lambda_c = 0.668 \mu\text{m}$ ,  $\Delta\lambda = 9 \text{ nm}$ ) filters after it has undergone the same optical path through the instrument. This results in the very similar diffraction and speckle pattern in both filters, allowing the continuum image to be used to remove the stellar contribution from the  $H\alpha$  image without affecting any potential line flux emitted from a protoplanet. Typical protoplanets do not contribute in the continuum image at  $\sim 0.65 \mu\text{m}$  due to their relatively low temperatures ( $\sim 1000$ – $2000 \text{ K}$ ) compared to stars. For more details on this observational mode and the reasoning behind it we refer the reader to Close et al. (2014a) and Cugno et al. (2019).

We obtained a total of 209 frames in each filter with a detector integration time of 60 s per exposure. Thanks to the high sky rotation rate, we achieved a total field rotation of  $\sim 106^{\circ}$ , ensuring a high throughput for the angular differential imaging (ADI; Marois et al. 2006) postprocessing algorithm.

### 2.2. HST/WFC3/UVIS

AS209 was observed with the HST/WFC3/UVIS instrument on 2023 May 3 for three orbits in the F656N ( $H\alpha$  narrow band,  $\lambda_c = 6561.5 \text{ \AA}$ ,  $\Delta\lambda = 17.9 \text{ \AA}$ ) filter using the UVIS2/C512C subarray (field of view =  $20''.5 \times 20''.5$ ). To improve the spatial sampling, a four-point dithering pattern was used, in which the telescope moves by 0.5 pixels between exposures. In total we obtained 108 frames of 13 s each, for a total time on target amounting to 23.4 minutes. In order to perform ADI, the roll angle in Orbit 2 differs by  $35^{\circ}$  from those in Orbits 1 and 3.

## 3. Data Reduction

### 3.1. MagAO-X

The MagAO-X data were reduced using the high-contrast imaging pipeline `PynPoint` (Amara & Quanz 2012; Stolker et al. 2019). After dark and flat calibration, frames are flipped along the  $x$ -axis to correct for a reflection within the instrument and bad pixels are corrected by  $4\sigma$  clipping. Images are then aligned to each other using cross-correlation and then centered by fitting a 2D Gaussian function to the mean image. The continuum and  $H\alpha$  frames were found to display an azimuthal offset of about  $0''.3$  and we corrected this by rotating the continuum images. This process resulted in squared images of  $3''.7$  in size (the MagAO-X pixel scale is  $0''.0059$ ).

We applied a frame selection based on the peak intensity of the point-spread function (PSF) in the  $H\alpha$  filter, measured in an aperture of radius  $0''.0135$  (2.3 pixels) in order not to be biased by the position of the star on the pixel grid. Since the instrument response to a point source is the same for every source, when the stellar PSF has a lower peak due to a low Strehl ratio, the same applies to faint protoplanet signals, making them more difficult to detect. We removed images with peak fluxes that deviated by  $> 2\sigma$  from the maximum value of the entire data set. This step removed 45 frames out of 209 from the data set, most of them temporally located toward the end of the night, when the weather conditions started to deteriorate.

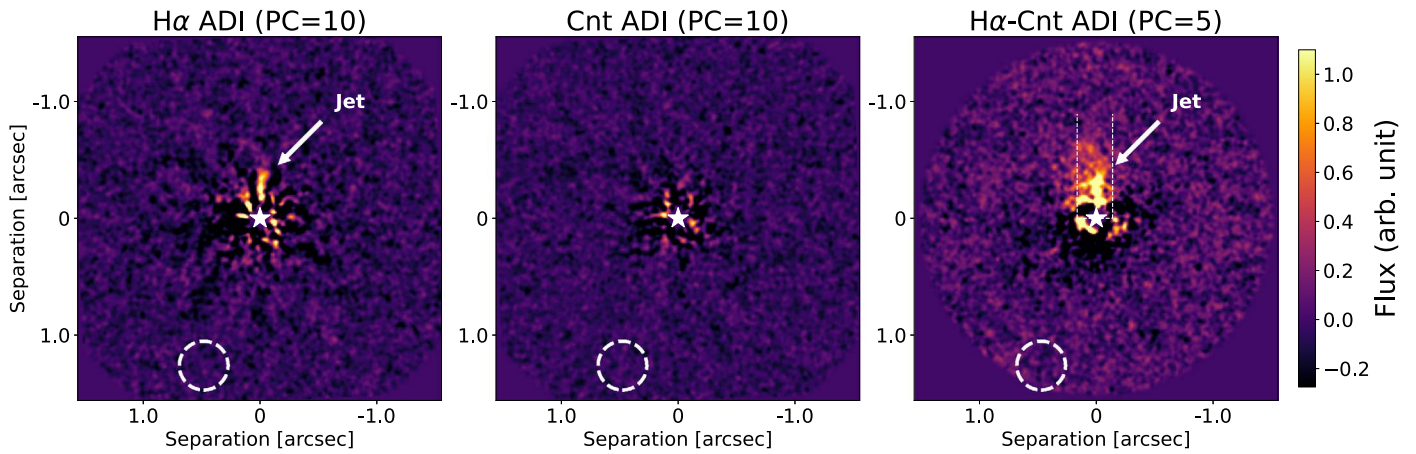


**Figure 1.** MagAO-X AS209 residuals in the H $\alpha$  (left panel), in the continuum (middle panel), and in the continuum-subtracted H $\alpha$  frames (right panel). North points to the top and east to the left. The white star indicates the position of the central star. The position of the CPD candidate is marked with a white dashed circle. The jet can be identified as the extended emission North of the star in both the left and the right panels. The rectangular mask applied for the jet brightness measurement is shown in the right panel.

Two different PSF subtraction techniques were applied. First, we removed the stellar PSF from individual filters (both H $\alpha$  and continuum) using ADI based on principal component analysis (PCA; Amara & Quanz 2012). We found that at least 10 principal components have to be subtracted in order to remove the bright stellar noise. Second, the PSF was removed using a combination of dual-filter differential imaging (Close et al. 2014a; Cugno et al. 2019) followed by ADI. The continuum frames are first spatially downsampled to match the PSF size (which is  $\propto \lambda$ ) at the H $\alpha$  wavelength<sup>18</sup> and their flux is upsampled by a factor 2.1 to match the total flux in the corresponding H $\alpha$  image within an aperture of  $r = 1''.0$ . This is necessary to compensate for the substantial line emission contribution due to stellar accretion in the H $\alpha$  filter. We found that the continuum subtraction accurately cancels most of the stellar noise, and only a few components have to be removed to reveal faint sources. After the final residuals were median combined, we applied a Gaussian filter of the size of the PSF (FWHM =  $0''.034$ ) to reduce pixel-to-pixel variations and highlight protoplanetary candidates.

### 3.2. HST

We initiated the data reduction process using the `flc` file obtained from the MAST archive. To begin with, we visually inspected the data in order to identify any hot pixels and cosmic rays present. These pixels were then replaced by employing linear interpolations based on the neighboring pixels. Subsequently, we reconstructed Nyquist sampled images by interlacing sets of four dithered images in Fourier space (for details on the image reconstruction we refer the reader to Lauer 1999; Zhou et al. 2021). This step resulted in 27 Nyquist sampled images with a pixel scale of  $0''.02$ .

For the primary subtraction, we again employed `PynPoint`. To align the images, we registered them according to the centroids of the PSFs, which were determined through 2D Gaussian fitting. The centroid-aligned image cube was then fed into the PCA algorithm, where images from one roll position are used to model and subtract the central PSF in the other roll position. For HST data, only a few components were removed.

<sup>18</sup> Information on the MagAO-X H $\alpha$  filters can be found at <https://magao-x.org/docs/handbook/observers/filters.html>.

Finally, after derotating and median combining the frames we applied again the high-pass filter (FWHM =  $0''.04$ ).

## 4. Results

The residual images (shown in Figures 1 and 2) do not reveal a signal at the location of the CPD candidate ( $1''.4$ , Bae et al. 2022b), and in Section 4.1 we calculate detection limits at the candidate location and discuss the nondetection. In addition, the residuals show extended emission north of the star coming from a jet both in the MagAO-X and HST data, as presented in Section 4.2.

### 4.1. AS209 b

The protoplanet candidate surrounded by a circumplanetary disk detected in  $^{13}\text{CO}$  by Bae et al. (2022b) was not detected, neither with MagAO-X nor with HST in H $\alpha$ . Its expected position is shown in the residual images of Figures 1 and 2.

To quantify the relevance of the nondetection, we estimated detection limits on the presence of H $\alpha$ -emitting sources. These were obtained with the `applefy` tool presented in Bonse et al. (2023) based on the metric proposed by Mawet et al. (2014). The detection threshold was fixed to a false-positive fraction (FPF) of  $2.87 \times 10^{-7}$ , equivalent to  $5\sigma$  for large separations and Gaussian noise. Artificial protoplanetary signals were inserted every  $0''.06$  at four different PAs. The planet signal and the noise were measured in an aperture of  $r = 3.2$  pixels and  $2.0$  pixels for the MagAO-X and HST data (half FWHM), respectively. For every separation the noise for 360 different aperture placements is estimated and we report the median over all results with the standard deviation representing the systematic uncertainty on the contrast measurement (see Bonse et al. 2023 for more details). Because the presence of the bright jet could bias the contrast curves, especially at short separations, we rotated the residuals in the opposite direction before combining them and estimating the noise (Pairet et al. 2019). This approach maintains the stellar and speckle noise, but avoids the presence of physical signals in the images used to sample the noise.

The obtained  $5\sigma$  contrast curves from MagAO-X data are shown in the left panel of Figure 3, in orange for the H $\alpha$ -Cnt, and in blue for the H $\alpha$  stack with PCA-ADI PSF subtraction.



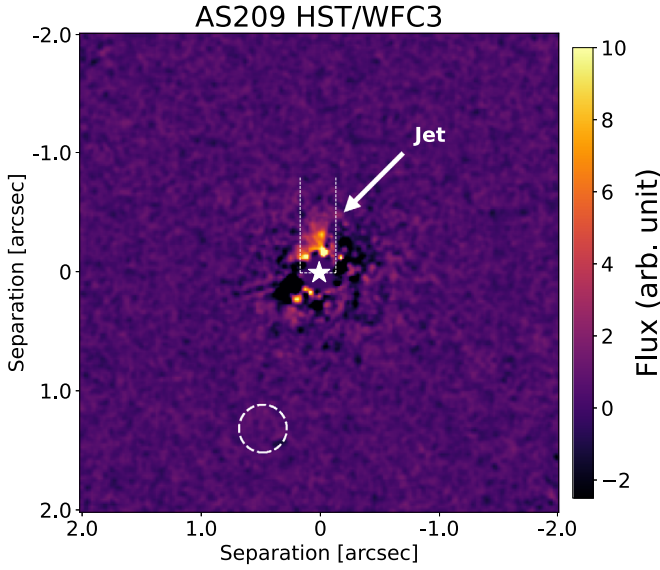


**Figure 2.** HST AS209 residuals in the F656N filter ( $H\alpha$ ). North points to the top and east to the left. The white star indicates the position of the central star, while the position of the CPD candidate is marked with a white dashed circle. The jet north of the star is re-detected in agreement with MagAO-X data. The rectangular mask applied for the jet brightness measurement is shown.

For the injection of planets we used the PSF from the continuum filter, as about 25% of the data in the  $H\alpha$  filter are saturated in the inner few pixels. In addition, stellar line emission may suffer from variability on different timescales and therefore the  $H\alpha$  flux is more difficult to calibrate. We note that the different filter throughputs might introduce a bias in the flux estimate of a few percent, much smaller than the contrast uncertainties. At small separations,  $H\alpha$  differential imaging outperforms ADI, providing contrasts  $\sim 1$  mag deeper. At larger separations, simple ADI reaches higher contrasts than  $H\alpha$  differential imaging. We attribute this behavior to the higher detector and readout noise introduced in the data by the continuum subtraction in the outer regions of the images, where the stellar emission does not dominate.

The contrast limits of the left panel of Figure 3 show that at the separation of the CPD candidate we reach a  $5\sigma$  contrast of  $11.5 \pm 0.1$  mag. For the absolute calibration, we adopted  $F_{\text{Cnt}}^* = 1.01 (\pm 0.1) \times 10^{-11} \text{ erg s}^{-1} \text{ cm}^{-2}$  for the stellar flux in the continuum filter of the MagAO-X data (Henden et al. 2015), where the 10% uncertainty was conservatively chosen to include potential variability (the nominal measurement uncertainty is 4%). Combining this value with the contrast limit measured for the CPD candidate, we obtained a  $5\sigma$   $H\alpha$  flux limit for the protoplanet of  $F_{\text{pl}}^{H\alpha} \lesssim 2.5 \pm 0.3 \times 10^{-16} \text{ erg s}^{-1} \text{ cm}^{-2}$ , which once corrected for the stellar distance ( $d = 121 \pm 0.4$  pc; Gaia Collaboration 2022) corresponds to a luminosity of  $L_{H\alpha}^{\text{obs}} \lesssim 1.15 \pm 0.15 \times 10^{-7} L_{\odot}$ . The overall luminosity upper limit as a function of separation from the MagAO-X data is shown in green in the right panel of Figure 3. At each separation, we adopted the higher contrast between the two curves reported in the left panel.

The contrast limits measured by HST are shown in the central panel of Figure 3. At the separation of the CPD candidate we reach a contrast of  $9.9 \pm 0.1$  mag. The contrast measured with respect to the stellar flux in the only HST filter available is not directly comparable to the one obtained above for the MagAO-X data for two reasons: (i) the HST filter is

centered on the  $H\alpha$  line, while for a more reliable flux calibration the MagAO-X contrast limits were measured with respect to the stellar flux obtained in the continuum filter, and (ii) the HST filter has a width of  $18 \text{ \AA}$ ,  $5\times$  smaller than the MagAO-X filters ( $\sim 90 \text{ \AA}$ ). From the HST images, we were able to measure the stellar flux in the F656N filter directly:  $3.22 \pm 0.05 \times 10^{-13} \text{ erg s}^{-1} \text{ cm}^{-2} \text{ \AA}^{-1}$ . Applying the contrast at the separation of the CPD candidate, we obtain a flux limit from the HST data of  $F_{\text{pl}}^{H\alpha} \lesssim 5.7 \pm 0.6 \times 10^{-16} \text{ erg s}^{-1} \text{ cm}^{-2}$ , and once corrected for stellar distance a luminosity upper limit of  $L_{H\alpha}^{\text{obs}} \lesssim 2.6 \pm 0.3 \times 10^{-7} L_{\odot}$ . These two quantities are directly comparable to the MagAO-X data, which provided lower limits and are able to exclude planets with dimmer luminosities. Hence, for the interpretation of the nondetection we will only focus on the upper limits provided by MagAO-X. A comparison of sensitivities achieved by the two observatories is further discussed in Section 5.4.

#### 4.2. Jet

Figures 1 and 2 reveal a jet north of the star imaged for the first time in AS209. Its extension in the 2D projected image goes up to a separation of  $0''.65$  in the MagAO-X data. The jet in the HST data is detected only up to  $0''.5$ , thus the values provided next only refer to the MagAO-X data. Assuming the jet is perpendicular to the disk plane, its physical extension is estimated to be  $\sim 169$  au. Its width in the residuals is  $\sim 0''.3$ , equivalent to  $\sim 36$  au at AS209's distance. This value is in line with the FWHMs of jets from other T Tauri stars (Ray et al. 2007). No receding jet is detected, possibly due to the obscuring effect of the circumstellar disk.

To estimate the jet profile, we applied a rectangular mask (width =  $0''.3$  for both instruments) to focus only on the image region with the jet signal (see the dashed lines in the right panel of Figure 1 and in Figure 2). To avoid the more aggressive subtraction induced by PCA, we used residuals produced with classical ADI: given the large field rotation in the MagAO-X data and the roll angle observing strategy used to obtain the HST data, we expect subtraction of the extended jet signal to be minimal (throughput  $\sim 100\%$ ) at large enough separations. However, some level of self-subtraction is expected in the innermost region of the images. In addition, those same regions suffer from strong speckle residuals from the PSF subtraction. Hence, we masked the inner  $0''.15$  in each data set. The flux from the jet was measured in annuli in steps of 1 FWHM ( $\sim 6.5$  pixels and  $\sim 4$  pixels for the MagAO-X and HST data, respectively), and normalized to the measurement area, obtaining the surface brightness profile. To calibrate the flux, we estimated the PSF counts within an aperture of  $2''.0$  and we compare it to the stellar flux as described in Section 4.1 to find a count-to-flux conversion factor for each instrument. The obtained conversion factors were applied to the brightness profiles, and the calibrated profiles are reported in Figure 4. The profiles estimated from the two instruments are in agreement. For the error bars, we considered two types of uncertainties. The first one, corresponding to the noise induced by stellar residuals, was estimated by considering the residuals outside the jet mask at the same separations and assigning an uncertainty to the measurement corresponding to the fraction of the noise counts over the jet counts (normalized by area). The second one corresponds to photon noise. At each separation we considered the largest source of uncertainty

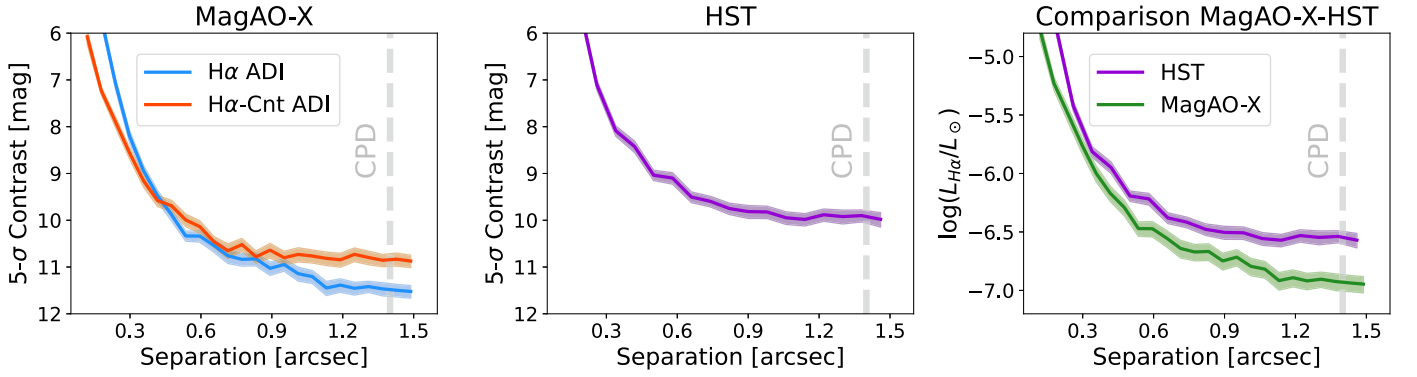


**Figure 3.**  $H\alpha$   $5\sigma$  contrast limits and  $H\alpha$  luminosity limits of AS209 as a function of separation. The gray dashed lines represent the separation of the CPD candidate (Bae et al. 2022b). Shaded regions represent the systematic uncertainty due to the speckle and residuals noise. Left: contrast curves obtained with MagAO-X. The curve obtained with the  $H\alpha$  differential technique is shown with an orange line, while the curve obtained with ADI PSF subtraction without continuum removal is shown with a blue line. Subtracting the scaled continuum improves the contrast performance by up to 1 mag, especially at short separations ( $\lesssim 0''.3$ ). Middle: contrast curves obtained with HST. Due to the different stellar fluxes in the filters used, the contrasts from the left and central panels are not directly comparable. Right:  $H\alpha$  luminosity upper limits as a function of separation for the two instruments; the curves are directly comparable, indicating that our MagAO-X data are more sensitive than our HST data at every separation in the image.

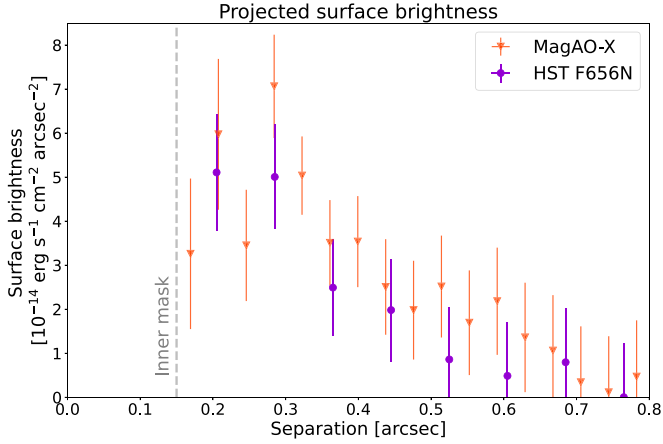


**Figure 4.** Surface brightness profile of the jet from AS209 as measured from MagAO-X (orange) and HST (violet) data. Error bars represent  $1\sigma$  uncertainties. The central mask with radius  $0''.15$  is shown with the dashed gray line.

(residuals  $\lesssim 0''.35$ , photon noise  $\gtrsim 0''.35$ ). The profiles obtained with the two instruments largely agree with each other.

The jet appears rather smooth and does not show significant knots as were observed for RY Tau (Garufi et al. 2019; Uyama et al. 2022) and HD163296 (Ellerbroek et al. 2014; Xie et al. 2021). However, it seems some intensity variation is present between  $0''.15$  and  $0''.3$  in the MagAO-X data, even though with the current data it is difficult to assess if the bumps in the profile are physical or due to the postprocessing.

## 5. Discussion

### 5.1. The Protoplanet Mass

AS209 has been observed with VLT/NaCo in the  $L'$  band as part of the NaCo-ISPYP survey (Launhardt et al. 2020). The data, presented in Cugno et al. (2023), exclude the presence of a companion brighter than 17.2 mag, which translates in an absolute magnitude of 11.8 mag at  $L'$ . Even though Cugno et al. (2023) showed the risk of using evolutionary models to transform IR brightness measurements into mass estimates, we use the detection limits to obtain a rough estimate of what NIR high-contrast imaging can exclude, assuming a clear view of the planet photosphere and no contribution of the accretion

luminosity at  $L'$ . For hot-start scenarios like AMES-Cond, NaCo limits exclude objects with  $M_p > 1.5 M_J$ , a very tight upper limit. However, for a colder scenario like the for the BEX-Warm models presented in Marleau et al. (2019) the mass limit is  $10.6 M_J$  (assuming an age of  $\tau = 2$  Myr), providing a much looser constraint. We note that a planet with such a high mass would have opened a much deeper and wider gap in the gas distribution of the disk than observed in  $^{12}\text{CO}$  (Kanagawa et al. 2015).

Bae et al. (2022b) used an empirical planet mass–gap width relation and calculated the mass of the planet embedded in the CPD candidate to be  $0.42\text{--}4.2 M_J$ , depending on the disk viscosity, assuming it is responsible for carving out the gas gap at  $\sim 200$  au. We note however that more recent work suggested that even lower masses are possible from a dynamical point of view. In fact, Galloway-Sprietsma et al. (2023) found disk winds emerging from the gap the CPD candidate is embedded in, and suggested that the kinematics could be dominated by the winds, not the planet. In this case, the planet mass inferred from the gap width could be overestimated. These mass estimates agree with the VLT/NaCo detection limits.

### 5.2. The Nondetection of the Candidate AS209 b

Different models can be used to transform measured  $H\alpha$  luminosities to mass accretion rates. Here, we compare two sets of models: the emission model of shock-heated gas for planetary mass objects (Aoyama et al. 2018, 2020), and the magnetospheric accretion model applied to planetary objects presented in Thanathibodee et al. (2019). Based on their non-local thermal equilibrium (non-LTE) models, Aoyama et al. (2021) determined the  $L_{H\alpha}\text{--}L_{\text{acc}}$  relation for protoplanets. Applying the relation to our measurement from Section 4.1, we obtain  $\log(L_{\text{acc}}/L_{\odot}) = -6.16 \pm 0.05$ . Following Gullbring et al. (1998), the mass accretion rate  $\dot{M}_{\text{acc}}$  can then be estimated with

$$\dot{M}_{\text{acc}} = \left(1 - \frac{R_p}{R_{\text{in}}}\right)^{-1} \frac{L_{\text{acc}} R_p}{GM_p}, \quad (1)$$

where  $R_p$  is the planet radius,  $R_{\text{in}}$  is the truncation radius of the disk, assumed to be  $\approx 5 R_p$ , and  $G$  is the gravitational constant. The mass of the planet has been assumed to be between  $0.5 M_J$

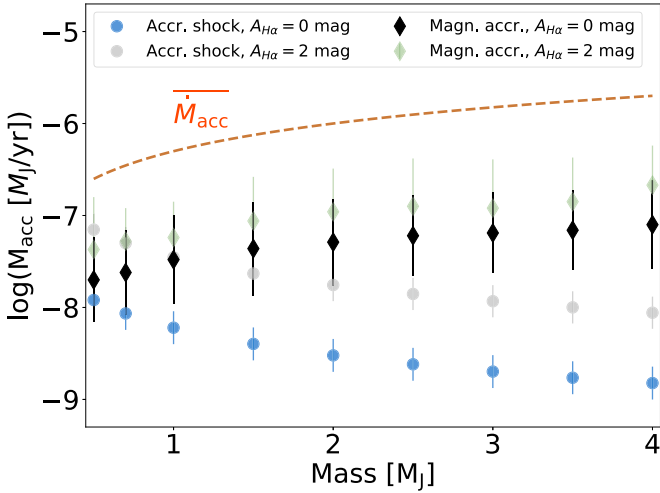


**Figure 5.** Mass accretion rate upper limit of the protoplanet candidate as a function of the planet mass  $M_p$  under different scenarios. The orange dashed line represents the average mass accretion necessary to build a planet of a given mass in 2 Myr. The blue and gray circles represent the mass accretion rate estimated using the shock-heated accretion models from Aoyama et al. (2021) using the observed  $H\alpha$  luminosity ( $A_{H\alpha} = 0$  and 2 mag, respectively). Black and green diamonds indicate the mass accretion rate when applying the magnetospheric accretion model for  $A_{H\alpha} = 0$  mag and 2 mag, respectively.

and  $4 M_J$  (see Section 5.1) and radii were drawn uniformly between 1 and  $3 R_J$ .

In order to consider magnetospheric accretion, we use the models from Thanathibodee et al. (2019) to generate a large grid of scenarios producing  $H\alpha$  lines. For each calculation, we systematically varied the planets’ and model’s parameters, encompassing a wide range of values whose boundaries are given either by the AS209 system’s possible properties or by extreme scenarios. Using masses between 0.5 and  $4 M_J$ , we adopted evolutionary models from Mordasini et al. (2017) to estimate radii for each mass consistent with 1–2 Myr ( $R_p$  in the 1.9–3.1  $R_J$  range). For a given set of mass and radius, we calculate a grid of 4050 models varying the magnetospheric parameters. The mass accretion rate  $\log(\dot{M}_{\text{acc}}/M_J \text{ yr}^{-1})$  was taken between  $-9$  (weak  $H\alpha$  produced) to  $-5$  (typical stellar accretion rate), the maximum flow temperature from 7000 K to 8000 K (lower temperatures do not produce  $H\alpha$ ),<sup>19</sup> the magnetospheric truncation radius from  $1.5 R_p$  (smaller values would bring the disk too close to the planet) to  $6 R_p$  (larger values require an unlikely strong magnetic field), flow width from  $0.5 R_p$  to  $2.5 R_p$  (similar to the stellar scenario), and the inclination from  $20^\circ$  to  $50^\circ$  (consistent with the circumstellar disk’s inclination). We then calculate the line luminosity from each model and select the model from which the luminosity is within  $1\sigma$  of the upper limits.

Initially, we did not consider extinction ( $A_{H\alpha} = 0$  mag). Figure 5 shows the mass accretion rate estimate as a function of the planet mass for the  $H\alpha$  limit of the CPD candidate. The orange dashed line represents the average mass accretion rate  $\overline{\dot{M}_{\text{acc}}}$  necessary to reach the planet mass on the  $x$ -axis in 2 Myr. As it is still unclear if and how accretion rates onto protoplanets evolve with time and on which timescales, we use  $\overline{\dot{M}_{\text{acc}}}$  as a proxy for a constant mass accretion rate over the stellar lifetime (2 Myr). If  $\dot{M}_{\text{acc}} > \overline{\dot{M}_{\text{acc}}}$ , then the planet is either undergoing a

period of vigorous (above average) accretion (meaning it underwent lower accretion in the past) or the planet’s age is lower than 2 Myr. If  $\dot{M}_{\text{acc}} < \overline{\dot{M}_{\text{acc}}}$ , then a large fraction of the planet mass was accreted in the past and currently the mass accretion rate is significantly lower than earlier phases. In Figure 5 the blue circles represent the distribution of possible  $M_p - \dot{M}_{\text{acc}}$  using the shock-heated gas models, while the black diamonds report the results from the magnetospheric accretion models.

The two models show different trends for increasing planet mass. The reason is that in the magnetospheric accretion model, to the first order, the line flux scales with the flow density  $\rho \propto \dot{M}/\sqrt{M_p}$  (Hartmann et al. 1994, Equation (9)) and hence for fixed line fluxes  $\rho$  does not vary and  $\dot{M}_{\text{acc}} \propto \sqrt{M_p}$ . Conversely, in the accretion shock models the freefall velocity of the infalling material is higher for a more massive planet, increasing the  $H\alpha$  flux. As a consequence, to produce the same  $H\alpha$  emission lower  $\dot{M}_{\text{acc}}$  is required at higher mass. The comparison between  $\overline{\dot{M}_{\text{acc}}}$  and the results for both sets of models suggests that the accretion rate is 10–100 times lower than  $\overline{\dot{M}_{\text{acc}}}$ . Hence, assuming no extinction, it seems the planet is accreting at a relatively low rate, indicating that in the past the accretion rate was likely much more vigorous.

However, circumstellar and circumplanetary material can strongly affect line emission at  $H\alpha$  wavelengths, especially in the presence of dust. Avenhaus et al. (2018) detected scattered light from the disk gap in AS209 indicative of the presence of small grains. Moreover, the nonzero disk inclination ( $i = 35^\circ$ ; Huang et al. 2018) possibly increases its effect on the detectable line emission. Unfortunately, the extinction properties of the outer regions of a circumstellar disk have never been measured, not to mention that we expect it to vary between sources and within individual sources depending on the location with respect to substructures and disk geometry.

From the nondetection of  $H\beta$  and the redetection of  $H\alpha$ , Hashimoto et al. (2020) constrained the extinction toward PDS70 b to be  $A_{H\alpha} \gtrsim 2$  mag, while Uyama et al. 2021 inferred  $A_V \approx 0.9$  and 2.0 mag for PDS70 b and c, respectively, considering the nondetection of  $\text{Pa}\beta$ . Following these estimates, we adopt here  $A_{H\alpha} = 2.0$  mag at the position of the CPD candidate, as it is located, similar to the PDS70 planets, in a deep gap, where the amount of small grains and pebble is expected to be relatively low (but not absent; see Avenhaus et al. 2018).

Including the effect of the extinction from the circumstellar disk material in the gap shifts the results from both models vertically along the  $y$ -axis of Figure 5. The new mass accretion rates are now closer to  $\overline{\dot{M}_{\text{acc}}}$ , but still 1–2 orders of magnitude lower. If this is the case, we conclude again that the protoplanet candidate accreted material much more vigorously in the first phases of its life (Lubow & Martin 2012; Brittain et al. 2020). The consequence of this early accretion scenario for direct imaging surveys of  $H\alpha$  emission would be drastic: at younger ages, when planets would accrete at larger rates, stars are still embedded in their envelopes and the direct detection of line emission would likely be hindered by the much larger extinction in the optical.

We note however, that the PDS70 planets (even though located in a different region of the disk) show signs of relatively strong accretion ( $>10^{-7} M_J \text{ yr}^{-1}$ ; Hashimoto et al. 2020; Zhou et al. 2021) at much older ages ( $\tau \sim 8$  Myr; Wang et al. 2021). If the protoplanet candidate continues to accrete

<sup>19</sup> We note this parameter is very uncertain even for the more studied case of accreting stars (Muzerolle et al. 2001).



material at least at a similar rate, an additional source of attenuation is needed to explain the nondetection, likely from circumplanetary material.<sup>20</sup> This scenario would be consistent with the interpretation of the <sup>13</sup>CO detection from Bae et al. (2022b), in which a circumplanetary disk surrounds the forming planet. We note that, under the assumption of a planetary atmosphere with physical and chemical properties similar to those of more mature planets, Cugno et al. (2021) estimated the extinction from the circumplanetary environment necessary to suppress molecular features from VLT/SINFONI data of PDS70 b to be  $A_V \approx 10\text{--}15$  mag ( $A_{H\alpha} \approx 8\text{--}12$  mag). For the same object, Wang et al. (2021) estimated the extinction from fitting the protoplanet’s spectral energy distribution with atmospheric models to be up to  $A_V \sim 10$  mag. A similar value for the extinction toward the protoplanet candidate would allow the  $L_{H\alpha}$  upper limits to be consistent with  $\dot{M}_{\text{acc}}$ . The much larger extinction from the CPD material is expected to suppress the  $H\alpha$  signal produced by accretion processes strongly. If this is the case, accretion tracers at longer wavelengths (e.g.,  $\text{Br}\gamma$  at  $2.16\ \mu\text{m}$  and  $\text{Br}\alpha$  at  $4.05\ \mu\text{m}$ ) could help reduce the effect of the extinction and confirm the presence of an accreting CPD.

A comparison of the CPD candidate around AS209 with the PDS70 planets reveals significant environmental differences that could explain the nondetection of the former and the multiple detections of the latter. The more advanced developmental stage of the PDS70 system potentially indicates a different evolutionary phase, wherein the planets may be less embedded compared to much younger protoplanetary disks like AS209, as with larger masses and longer times they are more capable of clearing gaps (Sanchis et al. 2020; Szulágyi & Ercolano 2020). Moreover, the presence of two planets inhabiting the same gap likely ensures an even higher level of gap clearing, thereby mitigating the effect of extinction on the emitted  $H\alpha$  flux. In order to characterize the evolution of forming planets thoroughly, a greater number of confirmed protoplanet direct detections is necessary, but the aforementioned dissimilarities suggest that distinct features are observable during the various phases of their formation.

### 5.3. A Jet in a Planet-forming Disk

Images of microjets (extensions  $\sim 100$  au) in Class II sources are relatively rare and are mostly confined to forbidden lines (Ray et al. 2007; Pascucci et al. 2023). However, microjets from T Tauri stars with high accretion rates are inferred to be common via spatially unresolved spectra of strong forbidden lines such as [O I] ( $\lambda 6300$ ) and [S II] ( $\lambda 6731$ ), where a “high-velocity component” is attributed to collimated outflowing gas with centroids around  $-100\ \text{km s}^{-1}$ , with the red side of the line occulted by the disk (Hartigan et al. 1995). In contrast, the detection of a microjet at  $H\alpha$  in a T Tauri star is usually prohibitive due to the high contrast required to distinguish it from the broad emission arising from magnetospheric accretion onto the star. As an example, for AS209 the equivalent width of  $H\alpha$  is  $113\ \text{\AA}$  and the line wings extend to  $\pm 300\ \text{km s}^{-1}$  (Alencar & Basri 2000). Instruments such as MagAO-X promise to be game changing for imaging microjets at  $H\alpha$  in accreting Class II sources that, in tandem with forbidden lines, will enable physical parameters, such as density, temperature, and mass ejection rates to be determined,

as is currently done for resolved jets from Class I and 0 sources (e.g., Nisini et al. 2005).

Of two published profiles of [O I]  $\lambda 6300$  in AS209, one from KECK’s HIRES spectrograph (Fang et al. 2018) and the other from Magellan’s MIKE spectrograph (Banzatti et al. 2019), only the second shows a high-velocity component associated with jet emission, while both show a low-velocity component associated with a slow, extended disk wind. Whether this is due to jet variability or to different slit alignments is unclear. The accretion rate for AS209 has been estimated from calibrated relationships between emission lines and accretion luminosity established from Balmer jump emission (Alcalá et al. 2017) to be  $\log(\dot{M}_{\text{acc}}/(M_{\odot}\ \text{yr}^{-1})) = -8.3$  (Fang et al. 2018), sufficiently high for jet emission to be expected (Nisini et al. 2018).

The receding jet was not detected, likely due to absorption from the protoplanetary disk material. Although receding jets are sometimes seen, (for example the Ae/Be star HD163296; see Xie et al. 2021), this is a relatively rare occurrence in T Tauri stars.

Future work with instruments like the Visible Integral-field Spectrograph eXtreme (VIS-X; Haffert et al. 2021) will be able to resolve the jet spectrally and spatially at  $H\alpha$ , allowing for the investigation of its velocity components. In addition, the calculation of ratios with other emission lines in the jet will enable the estimation of the level of ionization and thus jet mass-loss rate. Finally, an exciting prospect is the comparison between the stellar and the planetary mass accretion rates, once emission lines, possibly at longer wavelengths, will be detected.

### 5.4. The Future of Ground-based High-contrast Imaging in the Optical

The detection limits reported in Figure 3 show that in this case the data obtained with MagAO-X are more sensitive than those obtained from space with HST at every separation. Even though at least partially this is due to the very stable weather conditions during the observations and the longer amount of time spent on target (3.5 hours versus 23.4 minutes),<sup>21</sup> this work demonstrates the success of the recent efforts from the community to improve adaptive optics correction at short wavelengths. An additional point to consider is that AS209 is a relatively faint star ( $V = 11.3$  mag) and the adaptive optics correction will be even better for brighter targets like nearby stars. This is an exciting premise for the future development of ground-based high-contrast imagers like ELT/EPICS (Kasper et al. 2010) and GMagAO-X (Males et al. 2022b) that in the next decade will search for small terrestrial planets in reflected light.

## 6. Summary and Conclusions

We have observed AS209 with the MagAO-X instrument on the 6.5 m Magellan Clay telescope at Las Campanas Observatory in dual-imaging mode and with the HST/WFC3/UVIS camera in the F656N filter. We detected a collimated jet in  $H\alpha$ , which can be spectrally resolved with future observations to study the different velocity components. In addition, no signal from the CPD candidate proposed in Bae et al. (2022b) has been detected, suggesting that either the

<sup>20</sup> We note that Marleau et al. (2022) showed that accreting material only is not able to increase the extinction along the line of sight substantially.

<sup>21</sup> Note that including overheads, the amount of time used for the MagAO-X and HST observations is comparable, showcasing the efficiency of ground-based imaging.

instantaneous mass accretion rate is very low, or that local extinction from the circumstellar and circumplanetary environments is strongly attenuating line emission in the optical.

The interpretation of the protoplanet candidate orbiting AS209 and its mass accretion rate is highly dependent on the flux absorption. Our current inability to characterize the extinction from these elements accurately prevents us from further constraining the accretion onto the protoplanet candidate. Future observations should try to detect other hydrogen recombination lines in the NIR, where extinction plays a minor role. The comparison of line luminosities will further constrain the extinction from the line emitting region.











### Acknowledgments










G.C. thanks the Swiss National Science Foundation for financial support under grant number P500PT\_206785. Y.Z. acknowledges support from the Heising-Simons Foundation 51 Pegasi b Fellowship. This project has received funding from the European Research Council (ERC) under the European Union's Horizon 2020 research and innovation program (PROTOPLANETS, grant agreement No. 101002188). S.F. is funded by the European Union under the European Union's Horizon Europe Research & Innovation Programme 101076613 (UNVEIL). S.Y. H. was supported by NASA through the NASA Hubble Fellowship grant #HST-HF2-51436.001-A awarded by the Space Telescope Science Institute, which is operated by the Association of Universities for Research in Astronomy, Incorporated, under NASA contract NAS5-26555. L.C. and the MaxProtoPlanetS survey are supported by NASA eXoplanet Research Program (XRP) grant 80NSSC21K0397. L.A.P. acknowledges research support from the NSF Graduate Research Fellowship under Grant No. DGE-1746060. The results reported herein include data gathered with the Magellan Clay 6.5 m telescope located at Las Campanas Observatory, Chile. MagAO-X was developed under NSF MRI Award #1625441. The observations and data analysis works were supported by program HST-GO-17283. Some of the data presented in this paper were obtained from the Mikulski Archive for Space Telescopes (MAST) at the Space Telescope Science Institute. The specific observations analyzed can be accessed via <https://doi.org/10.17909/nf39-4h66>. Supports for Program numbers HST-GO-17283 were provided by NASA through a grant from the Space Telescope Science Institute, which is operated by the Association of Universities for Research in Astronomy, Incorporated, under NASA contract NAS5-26555.

*Facility:* Magellan: Clay (MagAO-X) and Hubble Space Telescope.

*Software:* PynPoint (Stolker et al. 2019) and applefry (Bonse et al. 2023).

### ORCID iDs

Gabriele Cugno  <https://orcid.org/0000-0001-7255-3251>  
 Yifan Zhou  <https://orcid.org/0000-0003-2969-6040>  
 Thanawuth Thanathibodee  <https://orcid.org/0000-0003-4507-1710>  
 Per Calissendorff  <https://orcid.org/0000-0002-5335-0616>  
 Michael R. Meyer  <https://orcid.org/0000-0003-1227-3084>  
 Suzan Edwards  <https://orcid.org/0000-0002-3232-665X>  
 Jaehan Bae  <https://orcid.org/0000-0001-7258-770X>  
 Myriam Benisty  <https://orcid.org/0000-0002-7695-7605>  
 Edwin Bergin  <https://orcid.org/0000-0003-4179-6394>  
 Matthew De Furio  <https://orcid.org/0000-0003-1863-4960>

Stefano Facchini  <https://orcid.org/0000-0003-4689-2684>  
 Jared R. Males  <https://orcid.org/0000-0002-2346-3441>  
 Laird M. Close  <https://orcid.org/0000-0002-2167-8246>  
 Richard D. Teague  <https://orcid.org/0000-0003-1534-5186>  
 Olivier Guyon  <https://orcid.org/0000-0002-1097-9908>  
 Sebastiaan Y. Haffert  <https://orcid.org/0000-0001-5130-9153>  
 Andrés Izquierdo  <https://orcid.org/0000-0001-8446-3026>  
 Joseph D. Long  <https://orcid.org/0000-0003-1905-9443>  
 Logan A. Pearce  <https://orcid.org/0000-0003-3904-7378>

### References

- Alcalá, J. M., Manara, C. F., Natta, A., et al. 2017, *A&A*, 600, A20  
 Alencar, S. H. P., & Basri, G. 2000, *AJ*, 119, 1881  
 Amara, A., & Quanz, S. P. 2012, *MNRAS*, 427, 948  
 Andrews, S. M., Huang, J., Pérez, L. M., et al. 2018, *ApJL*, 869, L41  
 Andrews, S. M., Wilner, D. J., Hughes, A. M., Qi, C., & Dullemond, C. P. 2009, *ApJ*, 700, 1502  
 Aoyama, Y., Ikoma, M., & Tanigawa, T. 2018, *ApJ*, 866, 84  
 Aoyama, Y., Marleau, G. D., Ikoma, M., & Mordasini, C. 2021, *ApJL*, 917, L30  
 Aoyama, Y., Marleau, G. D., Mordasini, C., & Ikoma, M. 2020, arXiv:2011.06608  
 Asensio-Torres, R., Henning, T., Cantalloube, F., et al. 2021, *A&A*, 652, A101  
 Avenhaus, H., Quanz, S. P., Garufi, A., et al. 2018, *ApJ*, 863, 44  
 Bae, J., Isella, A., Zhu, Z., et al. 2022a, arXiv:2210.13314  
 Bae, J., Teague, R., Andrews, S. M., et al. 2022b, *ApJL*, 934, L20  
 Banzatti, A., Pascucci, I., Edwards, S., et al. 2019, *ApJ*, 870, 76  
 Benisty, M., Dominik, C., Follette, K., et al. 2022, arXiv:2203.09991  
 Bonse, M. J., Garvin, E. O., Gebhard, T. D., et al. 2023, *AJ*, 166, 71  
 Brittain, S. D., Najita, J. R., Dong, R., & Zhu, Z. 2020, *ApJ*, 895, 48  
 Casassus, S., & Pérez, S. 2019, *ApJL*, 883, L41  
 Close, L. M. 2020, *AJ*, 160, 221  
 Close, L. M., Follette, K. B., Males, J. R., et al. 2014a, *ApJL*, 781, L30  
 Close, L. M., Males, J. R., Durney, O., et al. 2018, *Proc. SPIE*, 10703, 107034Y  
 Close, L. M., Males, J. R., Follette, K. B., et al. 2014b, *Proc. SPIE*, 9148, 91481M  
 Cugno, G., Patapis, P., Stolker, T., et al. 2021, *A&A*, 653, A12  
 Cugno, G., Pearce, T. D., Launhardt, R., et al. 2023, *A&A*, 669, A145  
 Cugno, G., Quanz, S. P., Hunziker, S., et al. 2019, *A&A*, 622, A156  
 Currie, T., Lawson, K., Schneider, G., et al. 2022, *NatAs*, 6, 751  
 Currie, T., Marois, C., Cieza, L., et al. 2019, *ApJL*, 877, L3  
 Dong, R., Liu, S. Y., & Fung, J. 2019, *ApJ*, 870, 72  
 Ellerbroek, L. E., Podio, L., Dougados, C., et al. 2014, *A&A*, 563, A87  
 Fang, M., Pascucci, I., Edwards, S., et al. 2022, *ApJ*, 868, 28  
 Fang, M., van Boekel, R., Wang, W., et al. 2009, *A&A*, 504, 461  
 Fernandez, M., Ortiz, E., Eiroa, C., Miranda, L. F., et al. 1995, *A&AS*, 114, 439  
 Flock, M., Ruge, J. P., Dzyurkevich, N., et al. 2015, *A&A*, 574, A68  
 Follette, K. B., Close, L. M., Males, J. R., et al. 2022, *AJ*, 165, 225  
 Gaia Collaboration, Vallenari, A., & Brown, A. G. A. 2023, *A&A*, 674, A1  
 Galloway-Sprietsma, M., Bae, J., Teague, R., et al. 2023, *ApJ*, 950, 147  
 Garufi, A., Podio, L., Bacciotti, F., et al. 2019, *A&A*, 628, A68  
 Gullbring, E., Hartmann, L., Briceño, C., & Calvet, N. 1998, *ApJ*, 492, 323  
 Guzmán, V. V., Huang, J., Andrews, S. M., et al. 2018, *ApJL*, 869, L48  
 Haffert, S. Y., Bohn, A. J., de Boer, J., et al. 2019, *NatAs*, 3, 749  
 Haffert, S. Y., Males, J. R., Close, L., et al. 2021, *Proc. SPIE*, 11823, 1182306  
 Hartigan, P., Edwards, S., & Ghandour, L. 1995, *ApJ*, 452, 736  
 Hartmann, L., Hewett, R., & Calvet, N. 1994, *ApJ*, 426, 669  
 Hashimoto, J., Aoyama, Y., Konishi, M., et al. 2020, *AJ*, 159, 222  
 Henden, A. A., Levine, S., Terrell, D., & Welch, D. L. 2015, AAS Meeting Abstracts, 225, 336.16  
 Huang, J., Andrews, S. M., Dullemond, C. P., et al. 2018, *ApJL*, 869, L42  
 Huélamo, N., Chauvin, G., Mendigutía, I., et al. 2022, *A&A*, 668, A138  
 Izquierdo, A. F., Facchini, S., Rosotti, G. P., van Dishoeck, E. F., & Testi, L. 2022, *ApJ*, 928, 2  
 Izquierdo, A. F., Testi, L., Facchini, S., et al. 2023, *A&A*, 674, A113  
 Kanagawa, K. D., Muto, T., Tanaka, H., et al. 2015, *ApJL*, 806, L15  
 Kasper, M., Beuzit, J. L., Verinaud, C., et al. 2010, *Proc. SPIE*, 7735, 77352E  
 Keppler, M., Benisty, M., Müller, A., et al. 2018, *A&A*, 617, A44



- Lauer, T. R. 1999, *PASP*, **111**, 227
- Launhardt, R., Henning, T., Quirrenbach, A., et al. 2020, *A&A*, **635**, A162
- Lubow, S. H., & Martin, R. G. 2012, *ApJL*, **749**, L37
- Males, J. R., Close, L. M., Haffert, S., et al. 2022a, *Proc. SPIE*, **12185**, 1218509
- Males, J. R., Close, L. M., Haffert, S. Y., et al. 2022b, *Proc. SPIE*, **12185**, 121854J
- Males, J. R., Close, L. M., Miller, K., et al. 2018, *Proc. SPIE*, **10703**, 1070309
- Marleau, G. D., Aoyama, Y., Kuiper, R., et al. 2022, *A&A*, **657**, A38
- Marleau, G. D., Mordasini, C., & Kuiper, R. 2019, *ApJ*, **881**, 144
- Marois, C., Lafrenière, D., Doyon, R., Macintosh, B., & Nadeau, D. 2006, *ApJ*, **641**, 556
- Mawet, D., Milli, J., Wahhaj, Z., et al. 2014, *ApJ*, **792**, 97
- Mordasini, C., Marleau, G. D., & Mollière, P. 2017, *A&A*, **608**, A72
- Muzerolle, J., Calvet, N., & Hartmann, L. 2001, *ApJ*, **550**, 944
- Nisini, B., Antonucci, S., Alcalá, J. M., et al. 2018, *A&A*, **609**, A87
- Nisini, B., Bacciotti, F., Giannini, T., et al. 2005, *A&A*, **441**, 159
- Öberg, K. I., Guzmán, V. V., Walsh, C., et al. 2021, *ApJS*, **257**, 1
- Pairat, B., Cantalloube, F., Gomez Gonzalez, C. A., Absil, O., & Jacques, L. 2019, *MNRAS*, **487**, 2262
- Pascucci, I., Cabrit, S., Edwards, S., et al. 2023, in ASP Conf. Ser. 534, *Protostars and Planets VII*, ed. S. Inutsuka et al. (San Francisco, CA: ASP), 567
- Pinte, C., Price, D. J., Ménard, F., et al. 2018, *ApJL*, **860**, L13
- Pinte, C., Price, D. J., Ménard, F., et al. 2020, *ApJL*, **890**, L9
- Pinte, C., Teague, R., Flaherty, K., et al. 2022, arXiv:2203.09528
- Ray, T., Dougados, C., Bacciotti, F., Eisloffel, J., Chrysostomou, A., et al. 2007, in *Protostars and Planets V*, ed. B. Reipurth, D. Jewitt, & K. Keil (Tucson, AZ: Univ. Arizona Press)
- Sallum, S., Follette, K. B., Eisner, J. A., et al. 2015, *Natur*, **527**, 342
- Sanchis, E., Picogna, G., Ercolano, B., Testi, L., & Rosotti, G. 2020, *MNRAS*, **492**, 3440
- Stolker, T., Bonse, M. J., Quanz, S. P., et al. 2019, *A&A*, **621**, A59
- Szulágyi, J., & Ercolano, B. 2020, *ApJ*, **902**, 126
- Teague, R., Bae, J., Aikawa, Y., et al. 2021, *ApJS*, **257**, 18
- Teague, R., Bae, J., Bergin, E. A., Birnstiel, T., & Foreman-Mackey, D. 2018, *ApJL*, **860**, L12
- Thanathibodee, T., Calvet, N., Bae, J., Muzerolle, J., & Hernández, R. F. 2019, *ApJ*, **885**, 94
- Tschudi, C., & Schmid, H. M. 2021, *A&A*, **655**, A37
- Uyama, T., Takami, M., Cugno, G., et al. 2022, *AJ*, **163**, 268
- Uyama, T., Xie, C., Aoyama, Y., et al. 2021, *AJ*, **162**, 214
- Wang, J. J., Vigan, A., Lacour, S., et al. 2021, *AJ*, **161**, 148
- Xie, C., Haffert, S. Y., de Boer, J., et al. 2020, *A&A*, **644**, A149
- Xie, C., Haffert, S. Y., de Boer, J., et al. 2021, *A&A*, **650**, L6
- Zhang, K., Blake, G. A., & Bergin, E. A. 2015, *ApJL*, **806**, L7
- Zhou, Y., Bowler, B. P., Wagner, K. R., et al. 2021, *AJ*, **161**, 244
- Zhou, Y., Sanghi, A., Bowler, B. P., et al. 2022, *ApJL*, **934**, L13
- Zurlo, A., Cugno, G., Montesinos, M., et al. 2020, *A&A*, **633**, A119